ORIGINAL PAPER

Mechanical properties and microstructure evolution of 1800 MPa grade low alloy ultrahigh strength steel during quenching and tempering process

Tong Wang[1] · Yang-xin Wang[1] · Chun-dong Hu[1,2] · Peng-min Cao[3] · Han Dong[1,2]

Abstract

The characterization techniques were employed like transmission electron microscope, X-ray diffraction and microstructural characterization to investigate microstructural evolution and impact of precipitate-phase precipitation on strength and toughness of a self-developed $32Si_2CrNi_2MoVNb$ steel during the quenching and tempering process. Research outputs indicated that the steel microstructure under the quenching state could be composed of martensite with a high dislocation density, a small amount of residual austenite, and many dispersed spherical MC carbides. In details, after tempering at 200 °C, fine needle-shaped ε-carbides would precipitate, which may improve yield strength and toughness of the steel. However, as compared to that after tempering at 200 °C, the average length of needle-shaped ε-carbides was found to increase to 144.1 ± 4 from 134.1 ± 3 nm after tempering at 340 °C. As a result, the yield strength may increase to 1505 ± 40 MPa, and the impact absorption energy (V-notch) may also decrease. Moreover, after tempering at 450 °C, those ε-carbides in the steel may transform into coarse rod-shaped cementite, and dislocation recoveries at such high tempering temperature may lead to decrease of strength and toughness of the steel. Finally, the following properties could be obtained: a yield strength of 1440 ± 35 MPa, an ultimate tensile strength of 1864 ± 50 MPa and an impact absorption energy of 45.9 ± 4 J, by means of rational composition design and microstructural control.

Keywords Strength · Toughness · Carbide · Microstructure · Evolution mechanism

1 Introduction

With the rapid development in fields such as aviation, aerospace, maritime, military, metallurgy, mining, petroleum, and power, there is a new demand for steel materials that are low-cost, low-energy consumption, ultra-high strength, ultra-high toughness, ultra-high wear resistance, and corrosion resistance. Both domestic and international efforts have been actively undertaken to research and develop ultra-high strength steel. As the demands for material performance continue to increase in modern industry, improving the strength and toughness of steel has become an important research direction. However, there is often a trade-off relationship between ductility and strength in most materials, where ductility decreases with increasing ultimate tensile strength [1]. By employing appropriate compositional design and material processing techniques, controlled precipitation phenomena can be induced, significantly enhancing the strength of the material. The ultimate tensile strength can be increased by up to 800 MPa, and the yield strength can exceed 1380 MPa [2–4]. Additionally, the Charpy V-notch impact absorption energy can be increased by more than 20 J [1, 5].

In order to develop steels with both ultra-high strength and good ductility, extensive research has been conducted. Martensitic steels are typical high strength materials that combine martensitic matrix with nano-precipitates [5]. However, these steels typically contain expensive alloying elements like Co (4%–15%), Mo (1%–5%), Ni (8%–18%),

---

Tong Wang and Yang-xin Wang contributed equally to this paper.

✉ Chun-dong Hu
hcd@shu.edu.cn

1   School of Materials Science and Engineering, Shanghai University, Shanghai 200444, China

2   Zhejiang Institute of Advanced Materials, SHU, Jiashan 314100, Zhejiang, China

3   Zhongyuan Special Steel Co., Ltd., Jiyuan 459000, Henan, China

Ti (0.2%–2%), in wt.%. For example, C350 steel [6], with relatively high commercialized strength (ultimate tensile strength of 2400 MPa) and 7% elongation, has the composition of C 0.03, Co 12, Mo 4.8, Ni 18.5, Fe balance, in wt.%. However, due to its high cost, it is challenging to widely use it in large quantities in industrial applications. To address this issue, efforts have been made to find methods to reduce the content of alloying elements. Wang et al. [7] utilized inexpensive and lightweight Al as a substitute for Co and Ti, forming strengthening precipitates. Compared to traditional martensitic steels, this approach offers advantages in terms of cost and weight, achieving an elongation of 8%. However, without the use of composite precipitates from other phases, it is challenging for this steel to reach ultimate tensile strength exceeding 1600 MPa. Additionally, it still contains 18% Ni and 4% Mo, resulting in high costs.

In recent decades, low-alloy ultra-high strength steel has attracted significant interest from researchers due to their low cost. These steels are quenched to form a martensitic structure at an appropriate temperature and then tempered at different temperatures to combine good strength, toughness, and fracture resistance properties [8]. Low-alloy ultra-high strength steels typically undergo low-temperature tempering in industrial applications, which allows them to achieve yield strengths exceeding 1 GPa and elongations exceeding 10%. This combination ultimately results in materials exhibiting ductile fracture behavior [9].

Wang et al. [5] developed a low-alloy ultra-high strength steel with ultrafine grain structure through a combination of Tempforming, which involves tempering and deformation of quenched steel, as well a low-temperature tempering after quenching. The main strengthening mechanisms in this steel include dislocation strengthening, precipitation strengthening, and grain refinement. Clarke et al. [8] conducted tempering experiments on 4340 steel at different temperatures and confirmed the presence of carbides in the tempered martensitic matrix. Complex precipitation structures were also detected. The study demonstrated the growth stages of carbides, with early growth potentially occurring under isothermal conditions, followed by the redistribution of alloying elements during the later growth process. Kawahara et al. [10] conducted research on the redistribution of carbon in quenched and tempered carbon steels and confirmed the dissolution and precipitation of ε-carbides. Xiong et al. [11] proposed an improved heat treatment process for DED-Arc 300M steel and explained that the main strengthening mechanisms were attributed to the strengthening solid-solution effect caused by carbon supersaturation and the coherent dispersion strengthening effect of fine ε-carbides.

This work investigated microstructural evolution and impact of precipitate-phase precipitation on strength and toughness of a self-developed 32Si$_2$CrNi$_2$MoVNb steel during the quenching and tempering process, which

primarily explored an effect of the tempering temperature on strength and toughness of such low-alloy ultra-high strength steel. This low-alloy ultra-high strength steel, 35Si$_2$CrNi$_3$MoVNb, usually exhibited superior performance compared to other similar steels, but remained a lower cost in economy. As a result, additions of microalloying elements V and Nb may work out carbonitrides which can inhibit the excessive growth of original austenite grains in the steel matrix. The addition of 2% Si in the studied steel effectively suppresses the formation of cementite at a tempering temperature of 340 °C, and the refined needle-like ε-carbides are beneficial to improving the toughness and increasing the tempering brittleness temperature of the steel. And, the absence of grain coarsening at an austenitizing temperature of 1020 °C can significantly improve strength and toughness of the steel. In addition, experimental testing was conducted on such specimens at both laboratory and industrial areas, and they have demonstrated excellent strength and toughness properties, with a strength value of 1830 MPa and impact toughness value (KV$_2$) of 49 J. In methodologies, microstructural evolution and precipitate-phase precipitation during the tempering for such steel were conducted by techniques like transmission electron microscopy (TEM), X-ray diffraction (XRD), and microstructural characterization. Through controlling chemical composition, microstructure, and carbides, this study would achieve breakthroughs in strength and toughness of low-cost low-alloy ultra-high strength steels, which may lay a theoretical foundation on design and development of such kinds of steels with outstanding performance.

2 Experimental

The steel has the nominal composition of Fe–0.32C–2.0Si–1.1Mn–0.6Cr–2.2Ni–0.3Mo–0.4 V (wt.%), which is smelted by the double vacuum process of vacuum smelting and vacuum self-consumption. The steel ingot obtained by smelting is of size ϕ570 mm × 2280 mm. Then, the ingot was forged at 1230 °C, and finally formed into an ingot with a diameter of 170 mm after three piers and three withdrawals. They were subsequently quenched at 1020 °C for 1 h, followed by oil quenching, and then tempered at 200, 340 and 450 °C for 2 h.

In order to investigate the mechanisms of strengthening and toughening through carbides and microstructural analysis in industrial steels, the microstructure of specimens tempered at different temperatures was characterized using a scanning electron microscope (SEM, Apreo 2S) and an electron backscatter diffraction (EBSD) instrument. The characterization was conducted at an operating voltage of 20 kV with a step size of 0.12 μm. EBSD data were reconstructed using the MTEX toolbox in Matlab software.

The impact test was conducted on an NI750 Charpy pendulum impact testing machine. The diameter of the tensile test specimen was 10 mm, with a gauge length of 100 mm. Uniaxial tensile tests were conducted using an Instron 5982 tensile testing machine with a strain rate of 10^{-3} s^{-1}. Figure 1 shows specimen dimensions under impact and tensile effects. The projection specimens were prepared using an electrolytic twin-jet and carbon replica method. The electrolytic twin-jet thinning apparatus (TJ-100SE) was employed for electrolytic twin-jet preparation at a temperature of −30 °C and an operating voltage of 30 kV. The carbon replica method involved carbon deposition on the specimens after corrosion with 4 vol.% nitric acid ethanol solution, followed by decarburization using 8 vol.% nitric acid ethanol solution. The morphology, size distribution, and crystal structure of carbides were characterized using TEM (JME-F2010) and a selected area electron diffraction instrument (SAED) at 200 kV. The dislocation density was characterized using an X-ray diffraction instrument (Rigaku D/Max-2550) under conditions of 40 kV, 200 mA, and a step size of 0.02°. Raw data obtained from XRD testing were smoothed by using the software Jade. Diffraction angle (2θ) and peak width (FWHM, $\Delta2\theta$) of (110) and (211) reflection peaks were then calculated [12].

For analyses of lattice strain and grain size, the Williamson-Hall equation was employed [13].

$$\frac{\Delta2\theta\cos\theta}{\lambda} = \frac{0.9}{D} + 2\varepsilon\frac{\sin\theta}{\lambda} \tag{1}$$

where λ represents the X-ray wavelength, 0.154 nm; D denotes the apparent grain size; and ε represents the lattice strain. The calculation formula for dislocation density ρ [14] was defined as $\rho = \frac{2\sqrt{3}\varepsilon}{Db}$, where b represents a magnitude of the Burgers vector.

3 Results and discussion

3.1 Mechanical property

Figure 2a shows a comparison of the ultimate tensile strength and Charpy impact absorption energy (V-notch) of the developed steel in this work (represented by red pentagrams) with other reported low-alloy ultra-high strength steels in industry [15–21]. The developed steel exhibited higher strength compared to the reported steels while still demonstrating good toughness. Figure 2b illustrates the relationship between tensile strength and elongation of the steel under different heat treatment conditions: quenched state (quenched at 1020 °C for 60 min) and tempered state (quenched and then tempered at 200, 340, and 450 °C for 120 min). RT stands for room temperature. Figure 2c shows the strength and impact absorption capacity of the steel in the quenched and tempered states. R_m represents ultimate tensile strength, while $R_{p0.2}$ represents yield strength. In the quenched state, the steel exhibited a yield strength of 1286 ± 32 MPa, ultimate tensile strength of 2110 ± 51 MPa, and impact absorption energy of 22.3 ± 3 J. After tempering, the mechanical properties of the steel were significantly improved. The yield strength had increased to 1440 ± 35 MPa, and the impact absorption energy had increased to 46 ± 4 J. However, the ultimate tensile strength had decreased to 1864 ± 50 MPa. With increasing tempering temperature, the ultimate tensile strength of the steel had gradually decreased from 2110 ± 51 to 1676 ± 45 MPa. As the tempering temperature increases, the yield strength had initially increased and then decreased. The impact absorption energy had initially increased and then decreased, ranging from 22.3 ± 3.1 to 45.9 ± 4.2 J, and then further decreased to 11.3 ± 2.5 J. The highest impact absorption energy was achieved at a tempering temperature of 200 °C. It is noteworthy that the developed steel achieved an excellent combination of strength and toughness. Compared to 4340 steel with a 2% addition of Si element, it surpassed the trade-off relationship typically observed in other reported low-alloy ultrahigh-strength steels. Figure 2d represents the yield strength increments curve (yield strength in the tempered state minus yield strength in the quenched state) from Fig. 2b. It could be observed that the yield strength increment occurred in two stages. When the tempering temperature was below 340 °C, the yield strength increment gradually increased with increasing tempering temperature. At a tempering temperature of 340 °C, the yield strength increment reached
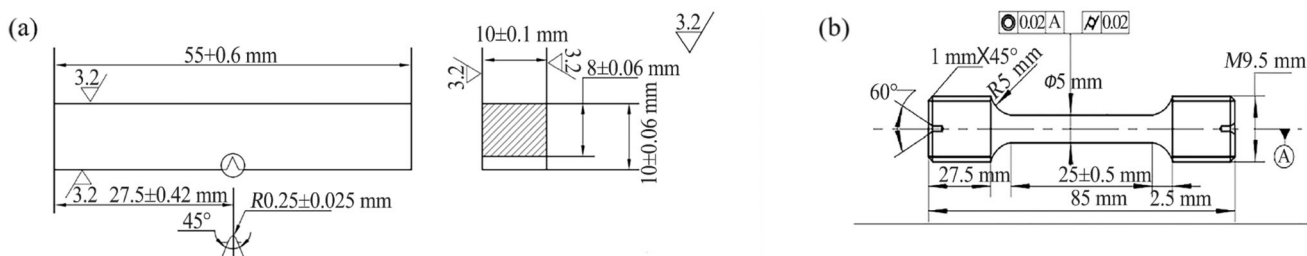

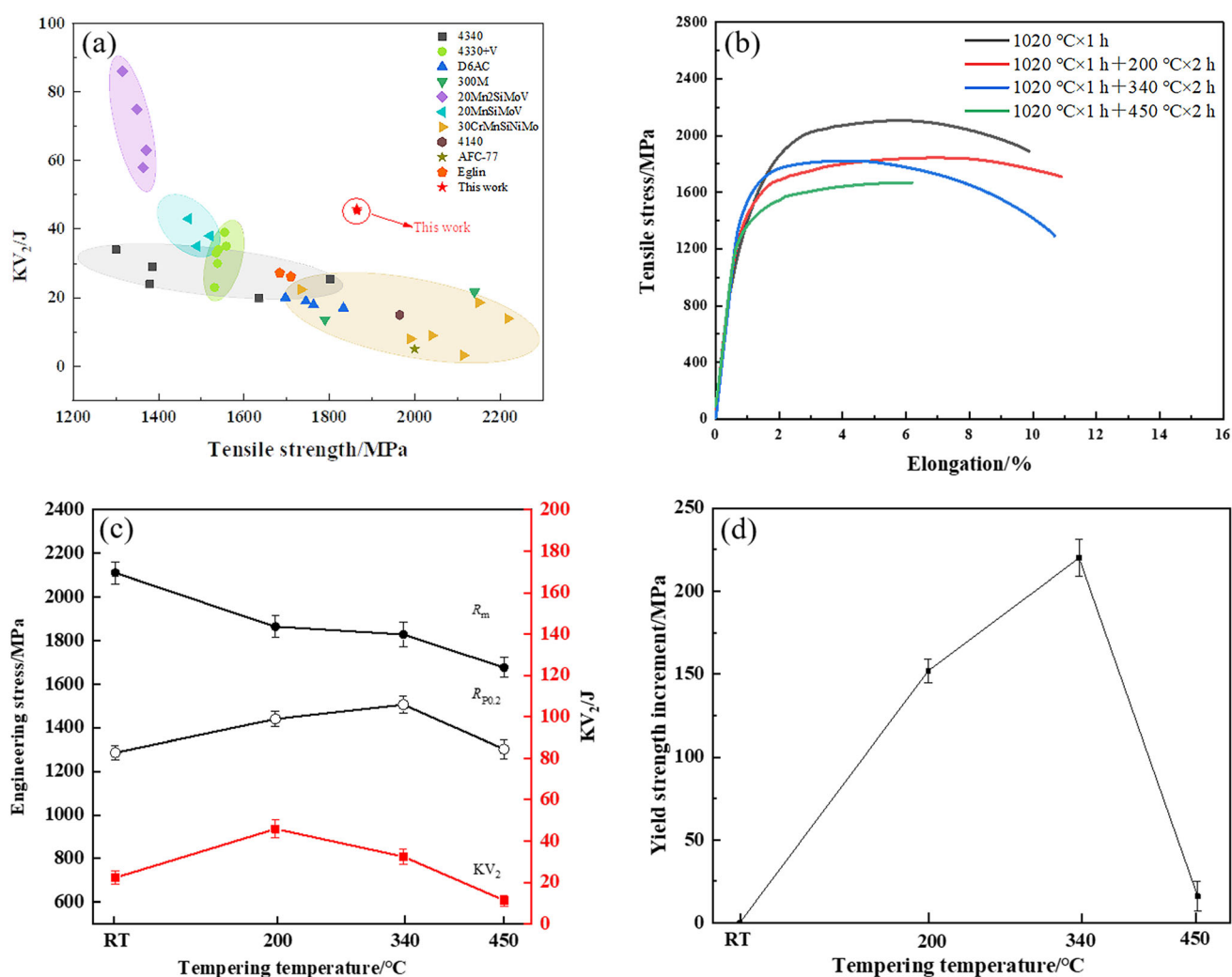**Fig. 1** Impact (**a**) and tensile (**b**) specimen size

Fig. 2 Statistical plot of tensile strength-impact absorption energy (V-notch) characteristics for different steels [15–21] (**a**), engineering stress–strain curve (**b**), statistical line plot of strength and impact absorption energy (V-notch) (**c**) and line plot of yield strength increment (**d**)

its highest value, increasing by 220 ± 11 MPa. When the tempering temperature was 450 °C, the yield strength increment decreased to 16 ± 9 MPa.

3.2 Microstructure characterization

Figure 3 presents the microstructure morphology of the steel under different heat treatment processes. The microstructure obtained from EBSD testing, as shown in Fig. S1, reveals a body-centered cubic (bcc) structure, suggesting that the microstructure of the steel in all conditions consisted of lath martensite. In the quenched state, the average width of the laths was 0.672 ± 0.1 μm, with the presence of spherical carbides ranging from 200 to 500 nm in diameter (Fig. 3a). After tempering at 200 °C, a small amount of needle-like carbides with length of 20–200 nm appear on the laths, and the average width of the laths is 0.668 ± 0.1 μm (Fig. 3b). Upon tempering at 340 and

450 °C, the lath boundaries become blurred, and the average widths of the laths are measured as 0.531 ± 0.1 and 0.567 ± 0.1 μm, respectively. At 340 °C, rod-like carbides with length ranging from 200–400 nm appear, and the amount of carbides increases (Fig. 3c, d). The lath widths of the martensite remain similar in different states, but with increasing tempering temperature, the lath boundaries become blurred, and carbides gradually precipitate. The steel used in this study exhibited a microstructure consisting of high-density lath martensite and a small amount of retained austenite in the quenched state. The size of the original austenite grains was determined to be 65.85 ± 5 μm, which can be confirmed in Fig. S2.

3.3 Dislocation evolution

Figure 4a displays XRD line profiles obtained from the steel after undergoing different heat treatment processes.
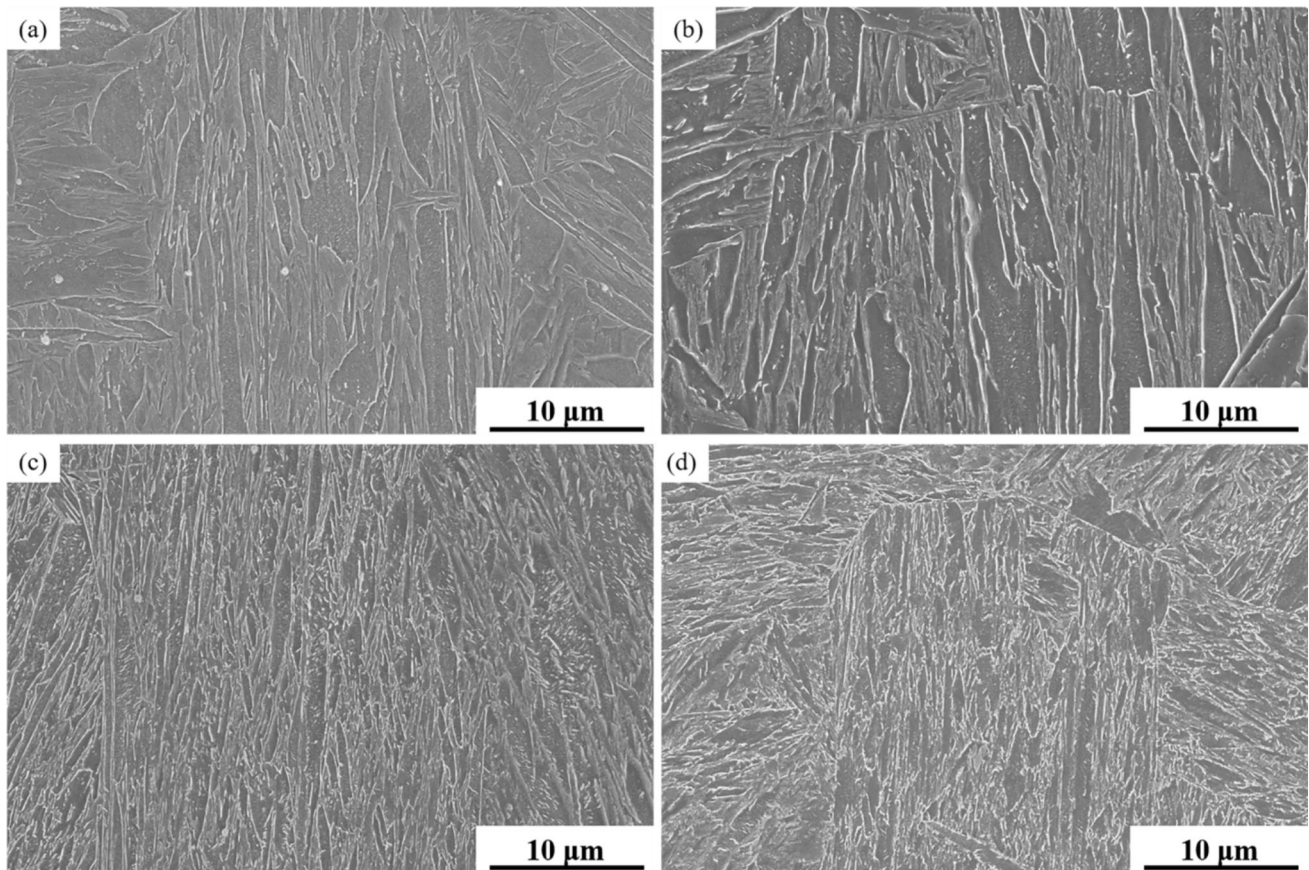
Fig. 3 Microstructural morphology of steel under different heat treatment processes. **a** Quenched state; **b** tempering at 200 °C; **c** tempering at 340 °C; **d** tempering at 450 °C

Figure 4b illustrates the Williamson-Hall plots. Figure 4c demonstrates the dislocation density obtained through XRD measurements. After tempering at 200 °C, the dislocation density of the steel would decrease from 2.6×10^{16} to 2.0×10^{16} m^{-2}. And, as the tempering temperature increased, the dislocation density would decrease as well. When the tempering temperature reached 450 °C, there would be a sudden drop of the dislocation density, reaching 6.4×10^{15} m^{-2}.

3.4 Mechanism of carbide evolution

Figure 5 illustrates TEM images of carbides under different tempering temperature. The carbides are marked with red arrows, and the diffraction patterns of the carbides are shown in the upper right corner of each image. Figure 5a shows TEM image of carbides in the quenched steel, which was made by carbon replica technique. Spherical carbides are observed in the quenched state. The diffraction pattern exhibits bcc structure with a zone axis of [110], which is designated as MC. The letter "M" represents the presence of Ti and V, which is confirmed by the energy spectrum of the carbides in Fig. S3. The average diameter of the

spherical carbides is 19.7 ± 2 nm. In Fig. 5b, TEM image shows the carbides after tempering at 200 °C. Lighter needle-like ε-carbides are observed, with a hexagonal structure. The carbides are uniformly distributed on the martensite lath, with a lath width of 668 ± 100 nm and an average carbide length of 134.2 ± 3 nm. Figure 5c displays the carbide morphology after tempering at 340 °C. Clearer needle-like carbides are observed on the martensite matrix, with an average length of 144.1 ± 4 nm. Figure 5d shows TEM image of carbides after tempering at 450 °C, which were made by carbon replica technique. Short rod-like carbides are observed, and the diffraction pattern indicates hexagonal structure and that the carbides are cementite. In Fig. 6a, the carbide distribution maps at different tempering temperatures are presented. At tempering temperatures of 200 and 340 °C, the carbide length distribution is concentrated in the range of 100–150 nm, accounting for 47.4% and 44.1%, respectively. At a tempering temperature of 450 °C, carbides with length greater than 300 nm appear, and the carbide size is predominantly distributed in the range of 100–250 nm. Figure 6b shows the statistical line graph of the average carbide length at different tempering temperatures. At 200 °C, the average
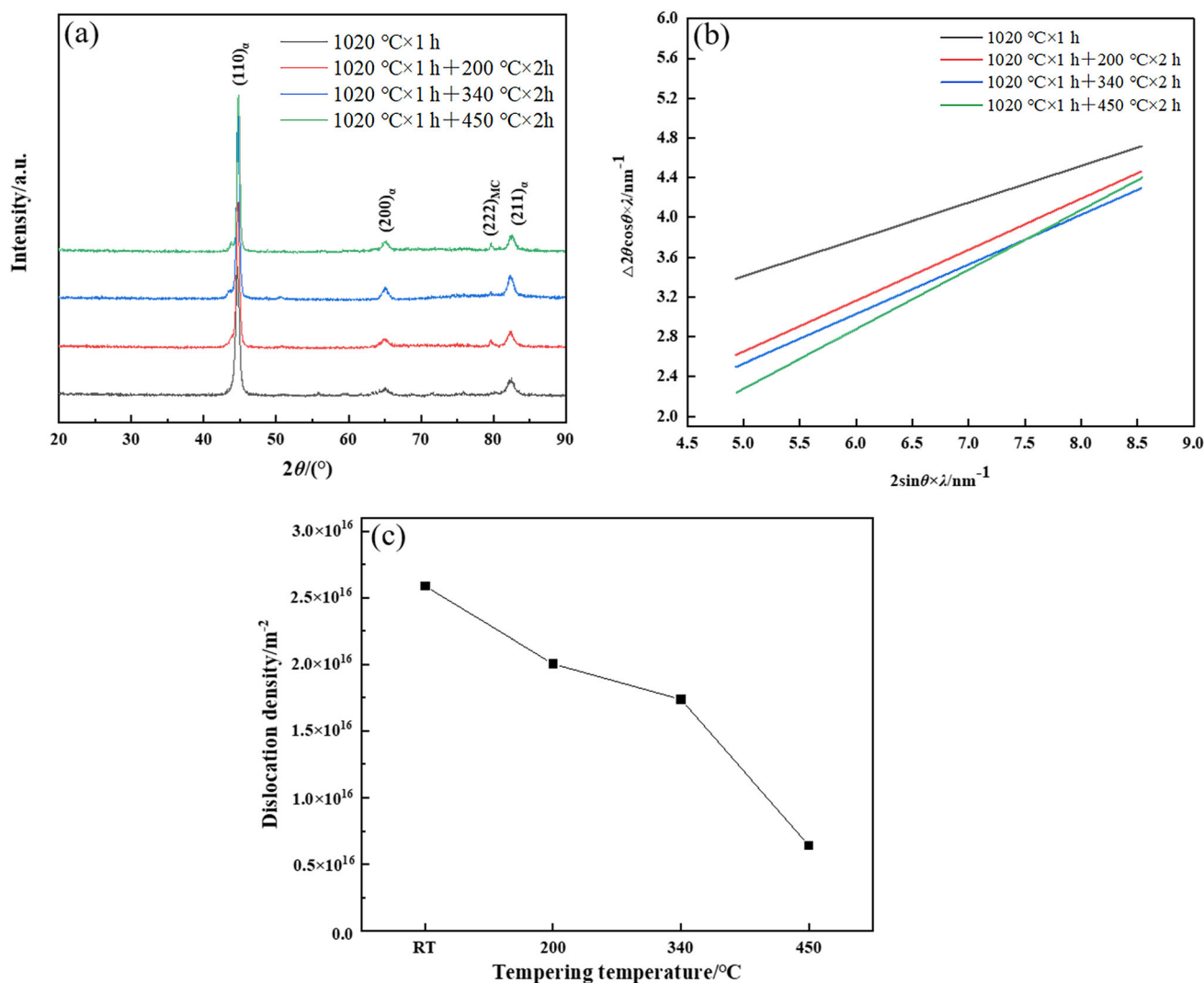
Fig. 4 XRD line profiles (raw data) (**a**), Williamson-Hall plots (**b**) and dislocation density of steel (**c**) under different heat treatment processes

carbide length is 134.2 ± 3 nm. As the tempering temperature increases to 450 °C, the carbides undergo rapid coarsening, and the average length increases to 212.2 ± 6 nm.

3.5 Fracture morphology

To further analyze the fracture characteristics, the surface morphology of the impact fracture surfaces of the steel after different heat treatment processes was observed using SEM, as shown in Fig. 7. The selected microstructures are from the crack propagation region. From Fig. 7a–c, small dimples can be observed, indicating a ductile fracture mode in the steel. After being subjected to tempering at 200 and 340 °C, the fracture surfaces exhibited larger and deeper dimples, with an average diameter of 3.18 ± 1 μm. In Fig. 7d, the fracture mode is characterized by intergranular fracture, exhibiting large-sized fracture features.

3.6 Evolution of microstructure and its relationship with strength and toughness

The width of the martensite laths and the size of the original austenite grains in the steel after different heat treatment processes showed little difference, and they had minimal impact on the strength and toughness of the steel. Due to the decomposition of martensite, the dislocation density decreased. Especially, when the tempering temperature reached 450 °C, the dislocation density would decrease from 2.6×10^{16} to 6.4×10^{15} m^{-2}. The reduction in dislocation density leads to a diminished dislocation strengthening effect, resulting in a decrease in tensile strength after tempering. After tempering, before the precipitation of carbides, the steel undergoes partial recovery of dislocations, which provides nucleation driving force for carbide precipitation [22].
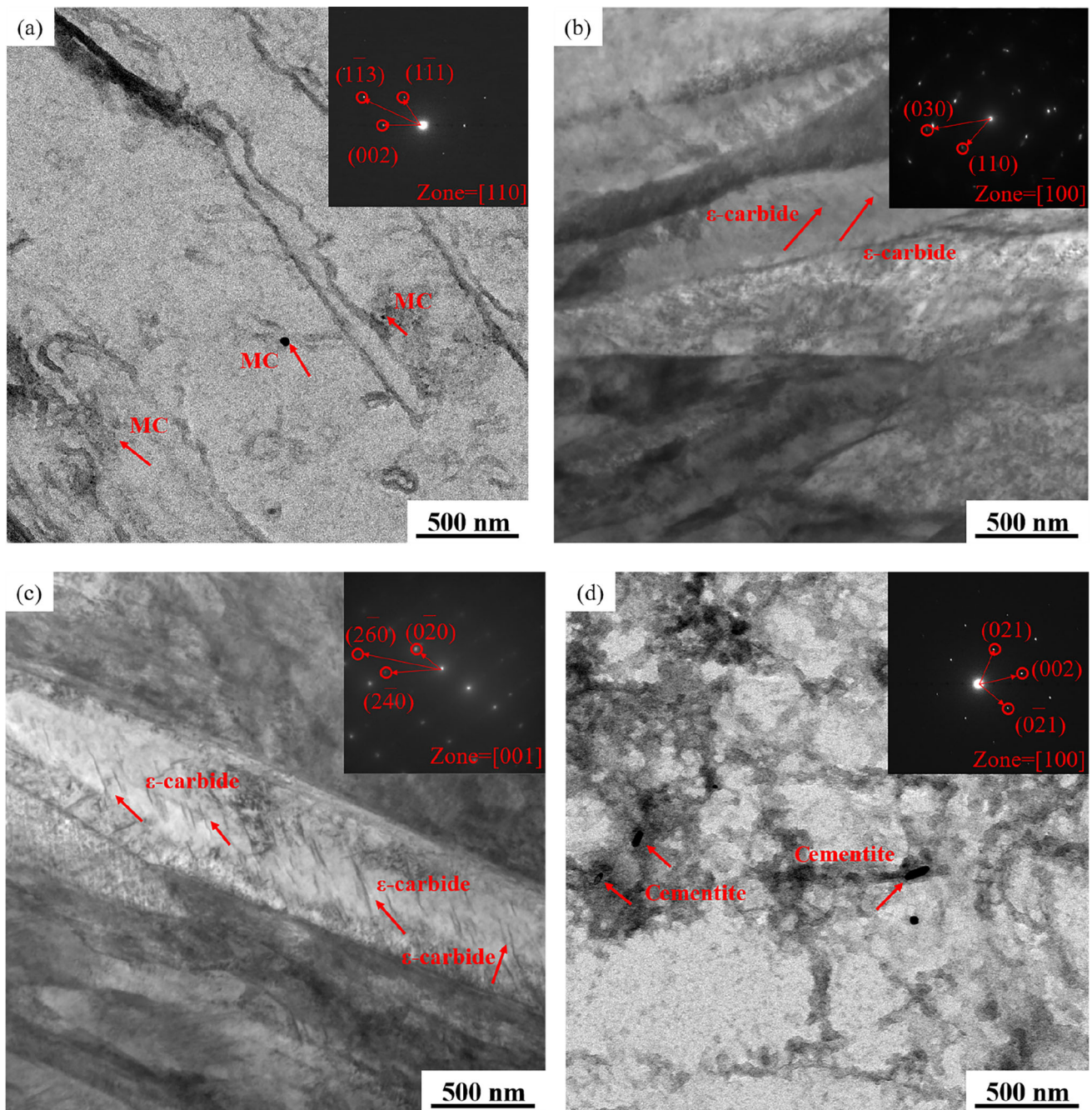
Fig. 5 TEM micrographs of specimens under different heat treatment conditions. **a** Quenched state; **b** tempering at 200 °C; **c** tempering at 340 °C; **d** tempering at 450 °C

3.7 Evolution mechanism of carbides and impact on strength and toughness

Compared to Fe_3C, ε-carbide exhibits a lower nucleation energy of 0.056 eV/atom [23–25], while Fe_3C has a higher nucleation energy of 0.124 eV/atom [26]. At lower tempering temperatures, ε-carbides with lower nucleation energy are more prone to nucleating. Therefore, at tempering temperatures of 200 and 340 °C, the predominant

precipitate phase in the microstructure is ε-carbide [27]. Therefore, at tempering temperatures of 200 and 340 °C, the predominant precipitates in the microstructure are ε-carbides. On the other hand, Fe_3C precipitation requires more energy and thus occurs at a higher tempering temperature of 450 °C. The high content of Si diffuses into ε-carbides, enhancing their stability and suppressing carbide coarsening, and thereby inhibiting the formation of Fe_3C. In comparison to 4340 steel, the addition of 2% Si in the
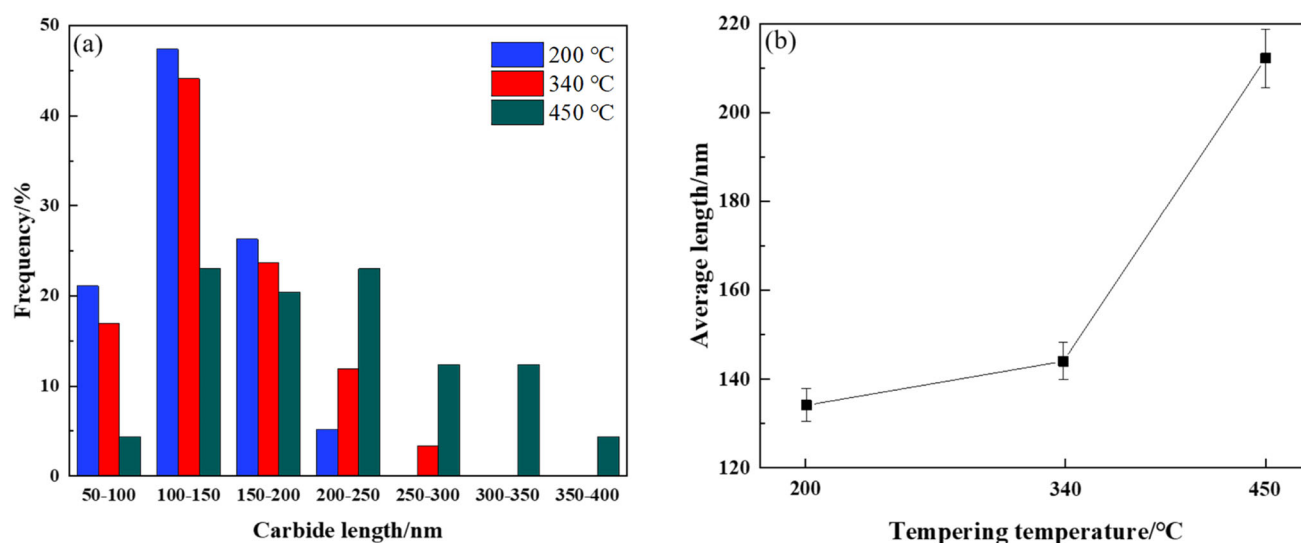
Fig. 6 Distribution map of carbides (**a**) and average size of carbides (**b**) at different tempering temperatures
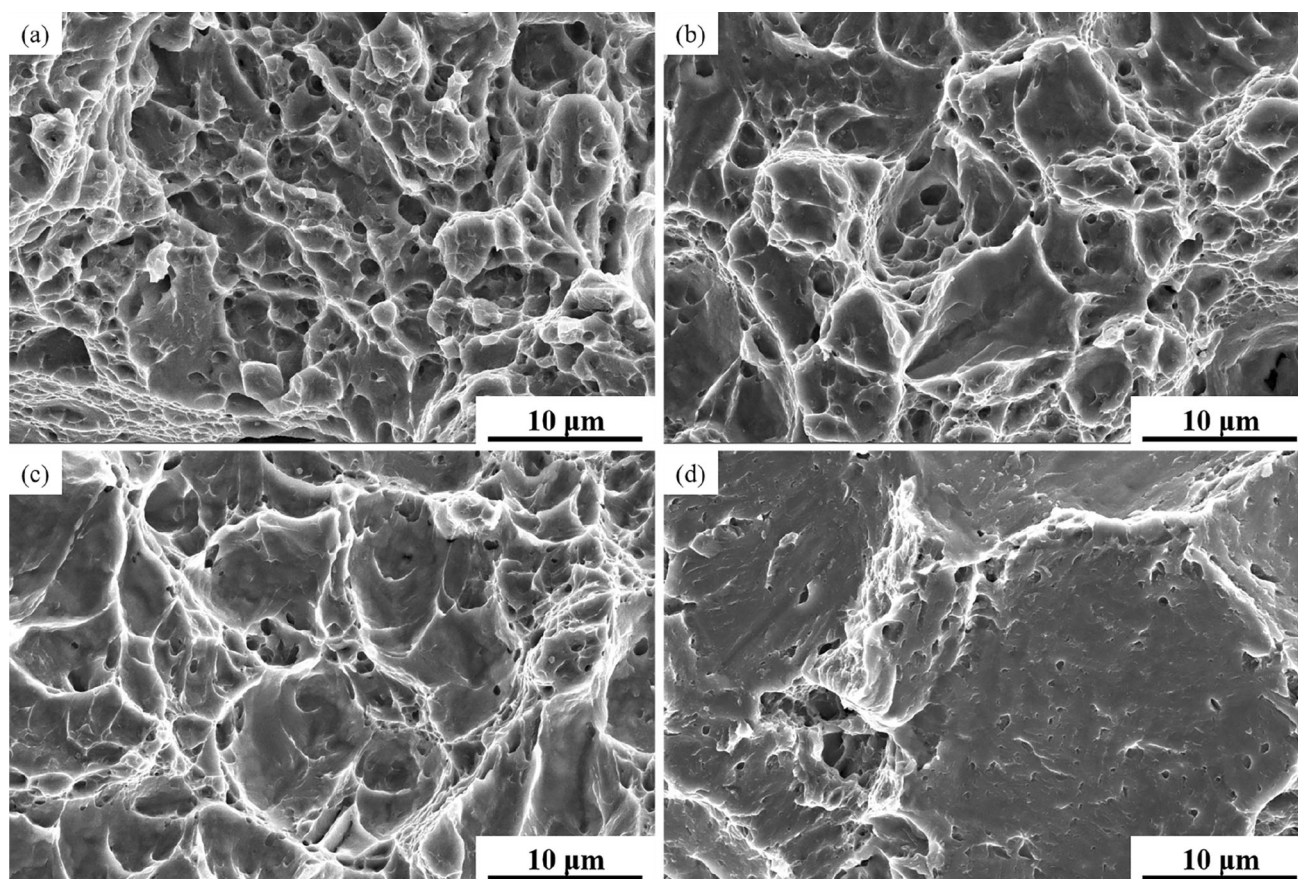

Fig. 7 Micrograph of impact fracture surface under quenched condition (**a**) and micrograph after tempering at 200 °C (**b**), 340 °C (**c**) and 450 °C (**d**)

steel that we investigated shifts the first-stage temper brittleness towards higher temperatures, enabling the steel to be tempered at higher temperatures and thereby improving its toughness.

From the results shown in Fig. 5, the spherical carbides observed on the martensitic matrix in the quenched state are primarily (V, Nb)C. Since MC carbides are relatively stable, they require higher temperatures to completely

decompose and dissolve into the matrix [28, 29]. Therefore, these carbides still exist during the tempering process, providing precipitation strengthening to the steel [30]. After tempering at 200 °C, needle-like ε-carbides with a hexagonal structure begin to precipitate between the martensite laths. The most densely packed planes and directions of the martensite and ε-carbide phases are nearly parallel, with a mismatch of only 1.2%. During low-temperature tempering, the surface energy of the martensite is maintained at a lower level as the carbides precipitate in the form of ε-carbides. ε-carbides primarily consist of Fe and C atoms. After the precipitation of carbides, the interstitial solid solution strengthening from carbon atoms in the steel is consumed [31], leading to a decrease in solid solution strengthening of the matrix. The interaction between precipitated ε-carbides and dislocations contributes to the strengthening effect. Due to the limited amount of precipitation at 200 °C, the yield strength increment is only 152 ± 7 MPa. As the tempering temperature reaches 340 °C, continuous precipitation of ε-carbides occurs, leading to coarsening to an average size of 144.1 ± 4 nm. The strengthening effect resulting from the high density distribution of ε-carbides interacting with dislocations progressively increases, resulting in a yield strength increment of 220 ± 11 MPa. This enhancement is attributed to the presence of 2% Si element in the steel. Si element effectively inhibits the growth of ε-carbides and their transformation into cementite, particularly in the vicinity of ε-carbide [32, 33].

Compared to 4340 steel tempered at 340 °C, ε-carbides have undergone complete transformation into cementite [34, 35]. Therefore, the presence of 2% Si in the steel studied effectively inhibits the formation of cementite at 340 °C. The presence of fine needle-like ε-carbides is advantageous for improving the toughness of the steel and raising the temper embrittlement temperature [32]. When the tempering temperature reaches 450 °C, ε-carbides in the steel completely disappear, and short rod-like cementite is formed. The formation of cementite consumes a significant amount of carbon atoms in the matrix, resulting in a decrease in solid solution strengthening [36–39]. Additionally, due to the reduction in dislocation density, the strength of the steel further decreases. This observation indicates that the strengthening effect of cementite is lower than the consumption of solid solution strengthening and dislocation strengthening. Simultaneously, cementite tends to precipitate at the grain boundaries and within the laths of the martensite. Larger-sized cementite particles are prone to accumulating at dislocations and other defects. During plastic deformation, moving dislocations can become entangled with cementite particles, leading to the formation of crack initiation sites and a reduction in the toughness of the steel [40]. Considering the microfracture surface depicted in Fig. 7, in the quenched state, uniformly distributed MC carbides in the steel tend to form small and shallow dimples, promoting toughness. When tempered at 200 °C, the presence of ε-carbides increases the size and depth of the dimples, which effectively hinders crack propagation and improves toughness. At a tempering temperature of 340 °C, the density of ε-carbides further increases, resulting in larger and deeper dimples. When the tempering temperature reaches 450 °C, an observation using Fig. S4 reveals the presence of a significant amount of carbides at grain boundaries and lath, which reduces the toughness of the steel.

After a certain extent of dislocation pile-up at the interface between the precipitate phase and the matrix, crack initiation occurs. Reducing the size of the precipitate phase and maintaining it at the nanoscale can mitigate the detrimental effect on the toughness of the precipitate phase, effectively enhancing toughness. The relationship between fracture toughness and the average spacing of second-phase particles, as proposed by Krafft's study, is expressed as follows [41]:

$$K_{IC} = nE\sqrt{2\pi l} \qquad (2)$$

where K_{IC} represents fracture toughness; n represents the quantity of precipitate phases; E denotes the elastic modulus of the material; and l represents the average spacing between precipitate phases. As the average spacing increases, K_{IC} also increases. At a tempering temperature of 200 °C, the steel exhibits an average spacing of ε-carbides of 171 ± 5 nm, which is greater than that at other tempering temperatures, resulting in the maximum fracture toughness.

4 Conclusions

1. The newly developed ultra-high strength steel, which incorporated 2% Si into the base 4340 steel, was produced under industrial conditions, resulting in a yield strength of 1440 ± 35 MPa, ultimate tensile strength of 1864 ± 50 MPa, and impact absorption energy of 45.9 ± 4 J per metric ton of material.

2. In the quenched state, the developed steel exhibited high dislocation density and strength, along with the strengthening effect of MC carbides. During tempering, as the microstructure decomposed, precipitate phases gradually formed. At tempering temperatures of 200–340 °C, the presence of fine ε-carbides improved the toughness and yield strength of the steel. However, at a tempering temperature of 450 °C, ε-carbides transformed into coarse rod-shaped cementite, leading to reduced toughness. Concurrently, the increase in

tempering temperature promoted dislocation recovery, resulting in a decrease in the strength of the steel.

3. This work demonstrates that breakthroughs in the strength and toughness of low-cost low-alloy ultra-high strength steels can be achieved through the control of chemical composition, microstructure, and carbides. It provides a theoretical foundation for the design and development of low-alloy ultra-high strength steels with even stronger performance.

Declarations

Conflict of interest The authors declare no conflict of interest.

References

[1] G.R. Speich, D.S. Dabkowski, L.F. Porter, Metall. Trans. 4 (1973) 303–315.

[2] W. Xu, P.E.J. Rivera-Díaz-del-Castillo, W. Yan, K. Yang, D. San Martín, L.A.I. Kestens, S. van der Zwaag, Acta Mater. 58 (2010) 4067–4075.

[3] Y. He, K. Yang, K. Liu, W. Sha, Z. Guo, Metall. Mater. Trans. A 37 (2006) 1107–1116.

[4] Y. He, K. Yang, W. Sha, Metall. Mater. Trans. A 36 (2005) 2273–2287.

[5] Y. Wang, J. Sun, T. Jiang, Y. Sun, S. Guo, Y. Liu, Acta Mater. 158 (2018) 247–256.

[6] S. Parvinian, D.E. Sievers, H. Garmestani, S.R. Kalidindi, Acta Mater. 215 (2021) 117071.

[7] Y. Wang, T. Deng, J. Zheng, Y. Qi, C. Xie, X. Zhou, G. Chen, Mater. Sci. Eng. A 871 (2023) 144884.

[8] A.J. Clarke, M.K. Miller, R.D. Field, D.R. Coughlin, P.J. Gibbs, K.D. Clarke, D.J. Alexander, K.A. Powers, P.A. Papin, G. Krauss, Acta Mater. 77 (2014) 17–27.

[9] M. Saeglitz, G. Krauss, Metall. Mater. Trans. A 28 (1997) 377–387.

[10] Y. Kawahara, K. Kaneko, H. Sawada, J. Takahashi, Acta Mater. 252 (2023) 118919.

[11] Y. Xiong, D. Wen, Z. Zheng, C. Sun, J. Xie, J. Li, Mater. Charact. 198 (2023) 112756.

[12] T. Koizumi, M. Kuroda, Mater. Sci. Eng. A 710 (2018) 300–308.

[13] G.K. Williamson, W.H. Hall, Acta Metall. 1 (1953) 22–31.

[14] G.K. Williamson, R.E. Smallman, Acta Crystallogr. 7 (1954) 574–581.

[15] O. Tikhe, P. Doiphode, U. Nichul, R. Singh, V. Hiwarkar, Met. Mater. Int. 29 (2023) 2216–2227.

[16] M.V. Maisuradze, Y.V. Yudin, A.A. Kuklina, Mater. Perform. Charact. 8 (2018) 20170168.

[17] M. Abdelwahed, S. Bengtsson, M. Boniardi, A. Casaroli, R. Casati, M. Vedani, Mater. Sci. Eng. A 855 (2022) 143941.

[18] K. Abbaszadeh, H. Saghafian, S. Kheirandish, J. Mater. Sci. Technol. 28 (2012) 336–342.

[19] M.V. Maisuradze, Y.V. Yudin, A.A. Kuklina, Metallurgist 63 (2019) 849–859.

[20] A. Zare, S.R. Hosseini, Int. J. Miner. Metall. Mater. 23 (2016) 658–666.

[21] G. Malakondaiah, M. Srinivas, P.R. Rao, Prog. Mater. Sci. 42 (1997) 209–242.

[22] M. Shamsujjoha, Mater. Sci. Eng. A 776 (2020) 139039.

[23] W.H. Zhang, Z.Q. Lv, Z.P. Shi, S.H. Sun, Z.H. Wang, W.T. Fu, J. Magn. Magn. Mater. 324 (2012) 2271–2276.

[24] H.L. Yakel, Int. Mat. Rev. 30 (1985) 17–44.

[25] Z.Q. Lv, F.C. Zhang, S.H. Sun, Z.H. Wang, P. Jiang, W.H. Zhang, W.T. Fu, Comput. Mater. Sci. 44 (2008) 690–694.

[26] S.B. Hendricks, Z. Für Kristallogr. Cryst. Mater. 74 (1930) 534–545.

[27] N.H. Heo, S.B. Kim, Y.S. Choi, S.S. Cho, K.H. Chai, Acta Mater. 51 (2003) 4953–4964.

[28] L. Sun, T.H. Simm, T.L. Martin, S. McAdam, D.R. Galvin, K.M. Perkins, P.A.J. Bagot, M.P. Moody, S.W. Ooi, P. Hill, M.J. Rawson, H.K.D.H. Bhadeshia, Acta Mater. 149 (2018) 285–301.

[29] K. Miyata, T. Kushida, T. Omura, Y. Komizo, Metall. Mater. Trans. A 34 (2003) 1565–1573.

[30] J. Hu, X. Li, Q. Meng, L. Wang, Y. Li, W. Xu, Mater. Sci. Eng. A 855 (2022) 143904.

[31] Y. Wang, T. Wang, C. Hu, Y. Mu, H. Zhao, H. Dong, Mater. Charact. 208 (2024) 113623.

[32] S. Teramoto, M. Imura, Y. Masuda, T. Ishida, M. Ohnuma, Y. Neishi, T. Suzuki, ISIJ Int. 60 (2020) 182–189.

[33] H. Sawada, N. Maruyama, S. Tabata, K. Kawakami, ISIJ Int. 59 (2019) 1128–1135.

[34] B. Kim, C. Celada, D. San Martín, T. Sourmail, P.E.J. Rivera-Díaz-del-Castillo, Acta Mater. 61 (2013) 6983–6992.

[35] D. Ning, C.R. Dai, J.L. Wu, Y.D. Wang, Y.Q. Wang, Y. Jing, J. Sun, Mater. Charact. 176 (2021) 111111.

[36] R.M. Horn, R.O. Ritchie, Metall. Trans. A 9 (1978) 1039–1053.

[37] M.R. Suresh, I. Samajdar, A. Ingle, N.B. Ballal, P.K. Rao, P.P. Sinha, Ironmak. Steelmak. 30 (2003) 379–384.

[38] R.C. Thomson, M.K. Miller, Acta Mater. 46 (1998) 2203–2213.

[39] W.J. Nam, H.C. Choi, Mater. Sci. Technol. 15 (1999) 527–530.

[40] V.K. Euser, D.L. Williamson, A.J. Clarke, J.G. Speer, JOM 74 (2022) 2386–2394.

[41] G.R. Irwin, J.M. Krafft, P.C. Paris, A.A. Wells, NRL Report 6598 (1967) 9–10.